Chapter 6

Growth of self-assembled ZnO nanoleaf from aqueous solution by pulsed laser ablation

§ 6.1 Introduction - ZnO

As an important II-VI semiconductor, zinc oxide (ZnO) has a direct band-gap (E_g = 3.37 eV) with a large exciton binding energy (60 meV), exhibiting near UV emission, transparent conductivity and piezoelectricity. Furthermore, ZnO is bio-safe and biocompatible, and may be used for biomedical applications without coating. Intensive research has been focused on fabricating 1D ZnO nanostructures and their morphologies with size-related optical and electrical properties [1,2,3]. Various kinds of ZnO nanostructures (figure 6.1), such as nanodots [4], nanowires (NWs) [5], nanorods (NRs) [6], nanobelts [7], nanorings [8], nanotubes (NTs) [9], nanocages [10] and hierarchical patterns, *etc*. [11] have been prepared by different methods. These techniques include chemical vapour transport and condensation (CVTC) [12], wet chemical methods [13], electrochemical deposition [14], template based growth [15], physical vapour deposition [16], metal-organic chemical vapour deposition (MOCVD) [17], and so on. With much progress being achieved in nearly all aspects of ZnO research, utilization of the excellent properties (semiconducting, piezoelectric, and pyroelectrical, optical) of ZnO have led to a wide variety of nanodevices in recently years, for instance ultraviolet photodetectors, sensors, field effect transistors, Schottky diodes and light emitting device arrays [18,19].
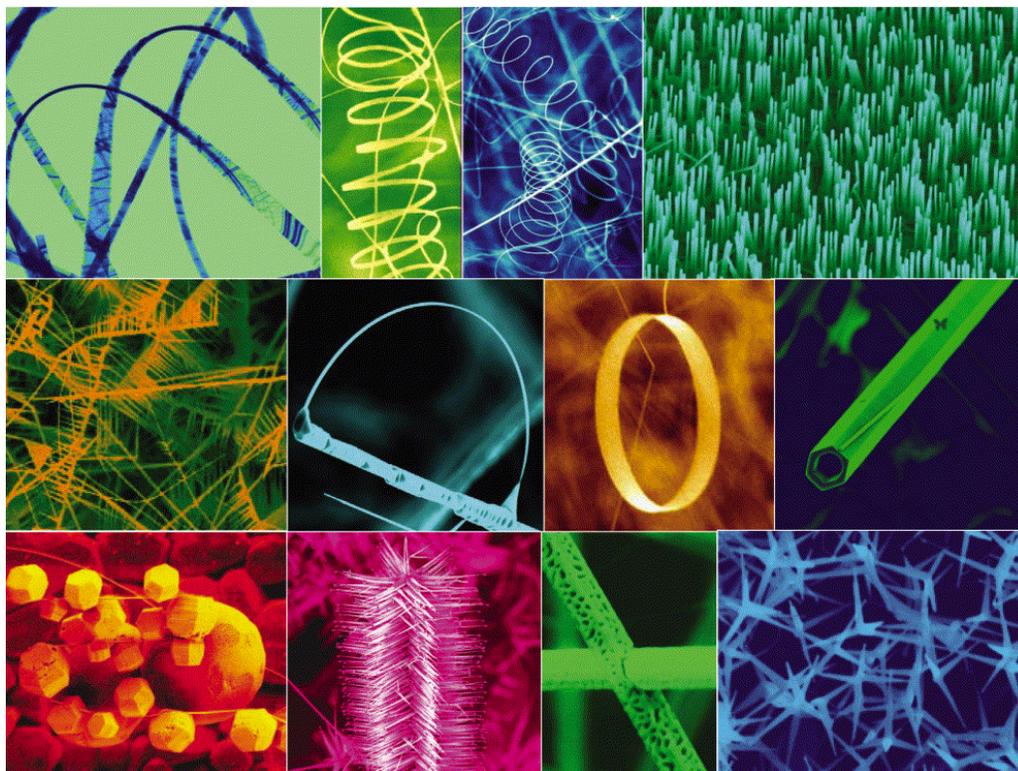
Figure 6.1   A collection of various nanostructures of ZnO [3].   Note this image is listed here only for illustration, scale bar is not shown.

§ 6.1.1   Crystal structure of ZnO

The crystal structures shared by ZnO are hexagonal wurtzite, cubic zinc blende, and cubic rocksalt.   At ambient conditions, the thermodynamically stable phase is the wurtzite structure.   Wurtzite zinc oxide has a hexagonal structure (space group *C6mc*) with lattice parameters $a = 0.3296$ and $c = 0.52065$ nm, which can be simply described as a number of alternating planes composed of tetrahedrally-coordinated O^{2-} and Zn^{2+} ions, stacked alternately along the *c*-axis (figure 6.2).   The tetrahedral coordination in ZnO results in a non-central symmetric structure and consequently piezoelectricity and pyroelectricity.   Another important characteristic of ZnO is polar surfaces.   The most common polar surface is the basal plane.   The oppositely charged ions produce positively charged Zn-(0001) and negatively charged O-($000\bar{1}$) polar

surfaces, resulting in a normal dipole moment and spontaneous polarization along the *c*-axis, as well as a divergence in surface energy. In wurtzite ZnO, besides the primary polar plane (0001) and associated direction <0001>, which are the most commonly used surface and direction for growth, many other secondary planes and directions exist in the crystal structure [20].
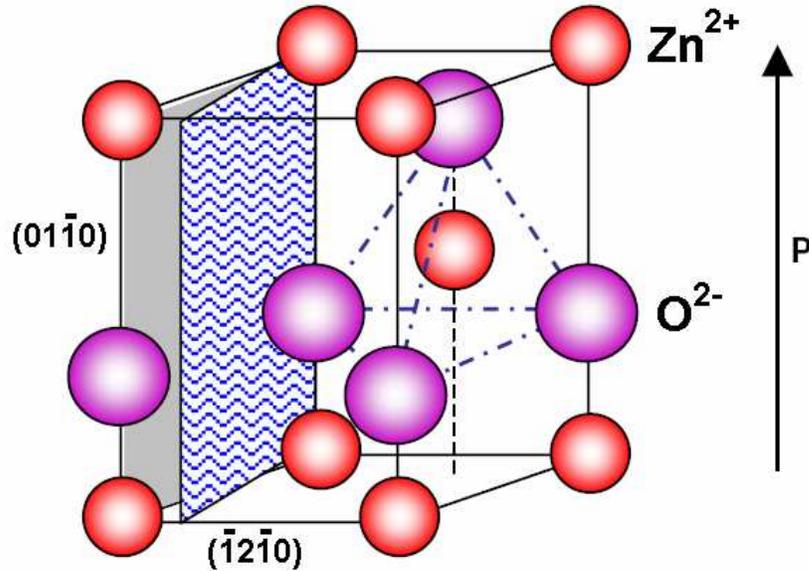

Figure 6.2 Wurtzite structure model of ZnO. The tetrahedral coordination of Zn-O is shown [12].

§ 6.1.2 Properties of ZnO

The properties of ZnO have been studied for many years, with most work focused on piezoelectric, hardness, thermal conductivity, optical and electron transport properties. Among reports of recent progress on the growth of a range of ZnO nanostructures, nanobelts and relevant nanostructures are a unique group that is likely to have important applications in nanosize electronic, optical, sensor and optoelectronic devices. A piezoelectric coefficient of a ZnO nanobelt has been measured by atomic force microscopy using a conductive tip [21]. On the basis of references of bulk (0001) ZnO and *x*-cut quartz, the effective piezoelectric

coefficient of the ZnO nanobelt was found to be frequency dependent and varied from 14.3 to 26.7 pm V^{-1}, which is much larger than the value for bulk (0001) ZnO of 9.93 pm V^{-1}. The results suggest application of ZnO nanobelts as nanosensors and nanoactuators.

Heat transport at the nanoscale is a very interesting and technologically important area. With the reduction of object size, phonon modes and phonon densities of states change drastically, resulting in unusual thermal transport phenomena in mesocopic systems. Kulkarni and co-workers [22] have measured the size-dependent thermal conductivity of zinc oxide nanobelts. The thermal conductivity of the nanobelts is significantly suppressed in comparison to that in the bulk due to increased phonon-boundary scattering and modified phonon dispersion [23]. This size effect can lead to localized heating in nanoelectronics [24], but may find potential use in improving thermoelectric performance.

ZnO nanostructures are the most promising materials for solid state chemical sensors, due to their small dimension, low cost, low power consumption and high compatibility with microelectronic processing. The fundamental sensing mechanism of metal oxide based gas sensors relies on a change in electrical conductivity due to the process of interaction between the surface complexes such as O^-, O^{2-}, H^+ and OH^- reactive chemical species and the gas molecules to be detected. Li and co-workers [25] have investigated electronic transport through individual ZnO NWs. UV illumination resulted in a jump in conductance by increasing the net carrier density and decreasing the depletion width. The conductance decreased with increasing oxygen pressure, indicating that the surface oxygen species controlled the electric transport through the individual ZnO NWs. These results demonstrated that individual ZnO NWs can be developed for room temperature gas sensors.

Optical transitions in ZnO have been studied by a variety of experimental techniques such as optical absorption, transmission, refection, photoluminescence (PL), cathodoluminescence, *etc*. As a direct and wide-band-gap material, ZnO is attracting a lot of attention. The strong exciton binding energy of ZnO, which is much larger than that of GaN (25 meV) and the thermal energy at room temperature (26 meV), can ensure an efficient exciton emission at room temperature under low excitation energy. As a consequence, ZnO is recognized as a promising photonic

material in the blue-UV region. Huang and co-workers [13] have demonstrated room temperature UV lasing of ZnO NRs synthesized by high temperature vapour-liquid-solid (VLS) growth methods. Figure 6.3 shows nearly all of the ZnO NRs grow vertically from the substrate with a diameter in the range from 60 to 80 nm (Figure 6.3(a)). PL spectrum of these NRs were measured with a He-Cd laser (325 nm) as an excitation source. Strong near-band-gap edge emission at ~ 377 nm has been observed. At low excitation intensity, the spectrum consists of a single broad spontaneous emission peak with a full width at half maximum of ~ 17 nm (line 1 in the Figure 6.3(b)). When the excitation intensity exceeds a threshold (~ 40 kW/cm^2), sharp peaks emerge in the emission spectrum (line 2 in the Figure 6.3(b)). The line widths of these peaks are < 0.3 nm, which are > 50 times smaller than the linewidth of the spontaneous emission peak below the threshold. The lasing threshold is quite low in comparison with previously reported values for random lasing (~ 300 kW/cm^2) in disordered particles or thin film [26], which make them ideal miniaturized laser light sources.
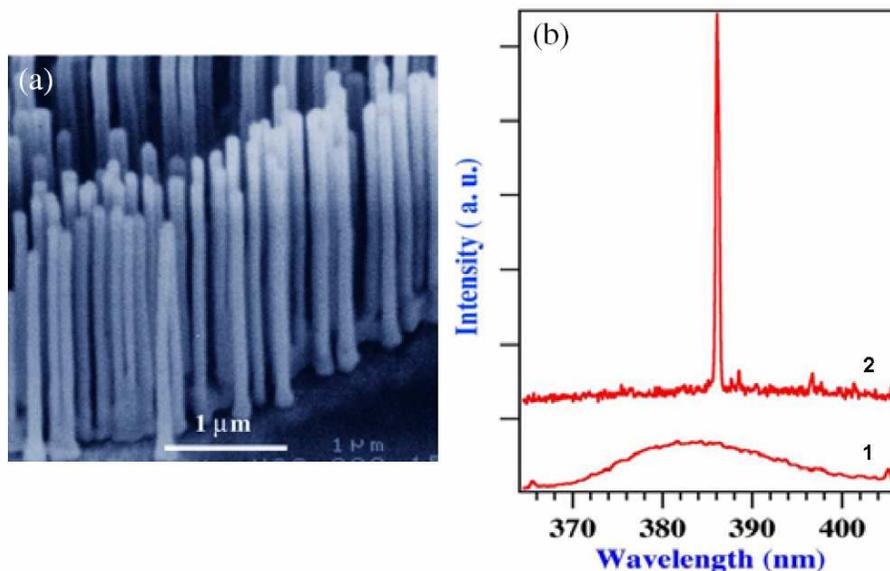

Figure 6.3 An SEM image of aligned ZnO NR arrays grown on a sapphire substrate coated with a 3 nm-thick layer of Au. (b) Emission spectra from NR arrays below (line 1) and above (line 2) the lasing threshold at pump power densities of 20 and 100 kW cm^{-2} using a Xe lamp with an excitation wavelength of 325 nm at room temperature [13].

Optically pumped stimulated emission with an excitonic origin has been observed by many researchers from ZnO epitaxial layers grown by a variety of methods. This is a vital first step for the realization of blue/violet laser diodes based on ZnO. Özgür and co-workers [27] have shown that ZnO layers deposited directly on *c*-plane sapphire substrates by radio frequency (RF) magnetron sputtering can have an optical quality sufficient for excitonic laser action. Stimulated emission and lasing from ZnO epitaxial layers, which can survive even at temperatures as high as 550 K have been observed by Bagnall and co-workers [28].

§ 6.1.3 Applications of ZnO

As mentioned previously, ZnO may have great potential in many practical applications due to its remarkable properties. For example, ZnO nanostructures have been used to fabricate a variety of nanodevices, such as ultraviolet photodetectors and light emitting device arrays. Recently, Kind and co-workers [29] reported the fabrication of ultraviolet photodetectors based on a single ZnO NW. The conductivity of the ZnO NWs was shown to be extremely sensitive to ultraviolet light exposure. The light-induced conductivity increase enables the NWs to be switched reversibly between 'OFF' and 'ON' states, demonstrating the possibility of creating highly sensitive NW switches based on the photoconducting properties of individual semiconductor NWs.

In 2001, a nanoscale coherent light source was firstly demonstrated in an optically pumped, room temperature ZnO NW ultraviolet laser. Since then, significant research efforts have been devoted to their optical characterization, lasing mechanisms and spectroscopic properties [30]. Fan and co-workers [31] reported the synthesis of single crystal ZnO NWs configured as field-effect transistors (FETs). Time resolved photocurrent measurements demonstrated that a ZnO FET can function as an optoelectronic switch.

ZnO NW humidity sensors had also been suggested by Wan and co-workers [32], demonstrating a very high sensitivity to ethanol vapour with a fast response time (within 10 s) at 300 ℃. Other gases, including H_2, O_2, and NO_2 [33,34,35], have been detected using ZnO sensors.

ZnO NRs are also starting to be used in the detection of biological molecules. Kim and co-workers [36] functionalized ZnO NR surfaces with biotin and developed nanosensors for the real-time detection of biological molecules using surface modified ZnO NRs as a conducting channel.

Another attractive application suggested for ZnO is its use as a catalyst, due to its high level of chemo-selectivity, high specific surface area, environmental compatibility, and simplicity of operation, as well as low cost. For example, Hosseini-Sarvari and co-workers [37] demonstrated that ZnO could act as an efficient and reusable catalyst for acylation of alcohols, phenols and amines under solvent free conditions. ZnO has also been reported as an alternative (and low cost) photo-catalyst to TiO_2 in the degradation of organic pollutants [38]. This could be important, since widespread use of TiO_2 catalyst is uneconomic for large scale water treatment operation.

§ 6.1.4 Aims of synthesis of ZnO nanostructures by LP-PLA

Although various synthetic routes (as mentioned in section 6.1) towards achieving controlled and reproducible growth of ZnO have been reported, the use of the LP-PLA technique to prepare ZnO nanostructures is relatively new. Compared to the conventional physical and chemical methods, the technique of LP-PLA has many distinct advantages: (i) a chemically "simple and clean" synthesis, the final product is usually obtained without byproducts and no need for further purification; (ii) low cost of experimental setup and easy controllable parameters; and (iii) the extreme confined conditions and induced high temperature, high pressure region favour the formation of unusual metastable phases. Therefore, LP-PLA is a technique which combines the merits of both physical and chemical methods, while giving high yield at low cost, and may be a feasible method to produce novel self assembled ZnO structures on an industrial scale.

Recently, the LP-PLA technique has been applied to zinc oxide by using a Zn target and an aqueous solution containing different surfactants. These surfactants stick to the charged particle surfaces, preventing further growth, and thereby aid the production of small particle sizes. For instance, Usui and coworkers [39] used the

surfactant cetyltrimethylammonium bromide (CTAB), lauryl dimethylaminoacetic (LDA) and octaethylene glycol monododecyl (OGM) to help form ZnO nanoparticles (NPs) with an average size of 12 nm. Also, Zeng and co-workers [40] used a solution of sodium dodecyl sulphate (SDS) to produce ~20 nm Zn/ZnO core-shell structure particles. These reports show that ZnO mainly forms zero-dimensional (0D) NPs by LP-PLA, although various approaches, including chemical vapour deposition, thermal evaporation, template-involved processes and solution-phase synthesis have been employed successfully for preparing more complex two-dimensional (2D) and three-dimensional (3D) superstructures of ZnO [41,42]. However, to the best of our knowledge, use of the LP-PLA technique has not yet been reported for the self-assembly of such complex ZnO structures.

Our recent findings [43,44,45,46] indicated that the instantaneous high temperature, high pressure and high density conditions that arise during LP-PLA can promote growth of crystalline carbon nitride nanomaterials (see Chapter 4 and Chapter 5). We demonstrated that the nanocrystals self-assemble into complex 2D and 3D architectures. Thus, a similar synthesis concept was extended to new, complex 2D nanostructures of ZnO fabrication, using an aqueous solution of SDS. This surfactant was chosen because it has been widely used in other systems, and it is known to affect the initial self-assembly process and also modify the resulting particle morphology [47].

§ 6.2 Experimental details of ZnO synthesis

99.99% Zn powder was compressed under (~ 10 kg cm^{-2}) pressure to form a solid target for ablation. Different ZnO nanostructures were prepared by LP-PLA in an aqueous solution with anionic surfactant SDS in a volume of 5 ml, using apparatus and methods that have been described in detail elsewhere (see Chapter 3 and [43]). Briefly, the laser beam was a Nd:YAG (532 nm, pulse duration 15 ns, frequency 10 Hz) with the power kept constant at 100 mJ per pulse, and focused through ~5 mm of the liquid onto a 0.5 mm-diameter spot on the ZnO target surface. All the laser ablation experiments were performed at room temperature and 1 atmosphere pressure. Different SDS concentrations (0.05-0.001 M) and ablation

times, t, (0.5-5 h) were investigated.   After ablation, the product was visible as a suspension of grey nanoparticles in the liquid.   In order to remove traces of SDS, the grey precipitates were washed several times with deionized water and ethanol, and then separated by centrifugation.

The solid precipitate samples were characterized and analysed by various techniques (see Chapter 3 for more details), including scanning electron microscopy (SEM), transmission electron microscopy (TEM) and high-resolution (HR) TEM. Powder X-ray diffraction (XRD) and selected area electron diffraction (SAED) were used to identify the zinc oxide phases.   Wavelength dispersed photoluminescence (PL) spectra were measured at room temperature following excitation with a c.w. He-Cd laser ($\lambda = 325$ nm, power ~3 mW).   An ultraviolet-visible (UV-vis) spectrophotometer was used to monitor the changes in absorbance of the ablated solution.   The X-ray photoelectron spectroscopy (XPS) measurement used Al-Kα (1486.6 eV) radiation operating at 400 W (15 kV).   High resolution scans were acquired with 30 eV pass energy and 200 ms dwell times.

§ 6.3 Growth of self-assembled ZnO nanoleaf structures

§ 6.3.1 General features of ZnO nanostructures

As laser irradiation progressed, the liquid changed from colourless to a grey coloured suspension, indicating an increase in solid product and/or a change in composition of the solid due to interaction with the laser. A typical XRD study in Figure 6.4(a) shows that the prepared samples were consistent with the ZnO wurtzite phase (P6$_3$mc(186), JCPDS card no. 36-1451) with lattice constants $a_0 = 3.2498$ Å and $c_0 = 5.2066$ Å [48]. One-dimensional spherical particles (Figure 6.4(b)) of size ~5-25 nm appeared after only 30 min ablation in 0.01 M SDS. When increasing the laser ablation time to 2 h, the crystallites had elongated into rod-like structures, as shown in Figure 6.4(c). The elongation mechanism is still unclear, but Figure 6.4(c) shows that some adjacent particles (highlighted by arrows) may be lining up. This suggests that the nanorods (NRs) may be the result of individual pre-formed NPs

adding preferentially to the ends of a line of NPs (Figure 6.4(d)). Alternatively, NRs may form by 1D growth of a single NP, but we have not yet found any evidence for this. Whichever mechanism is correct, it is clear that NR formation, growth and aggregation all occur after only a short ablation time. This is consistent with the findings of Zeng *et al* [49], who observed NPs of ZnO after short duration LP-PLA.
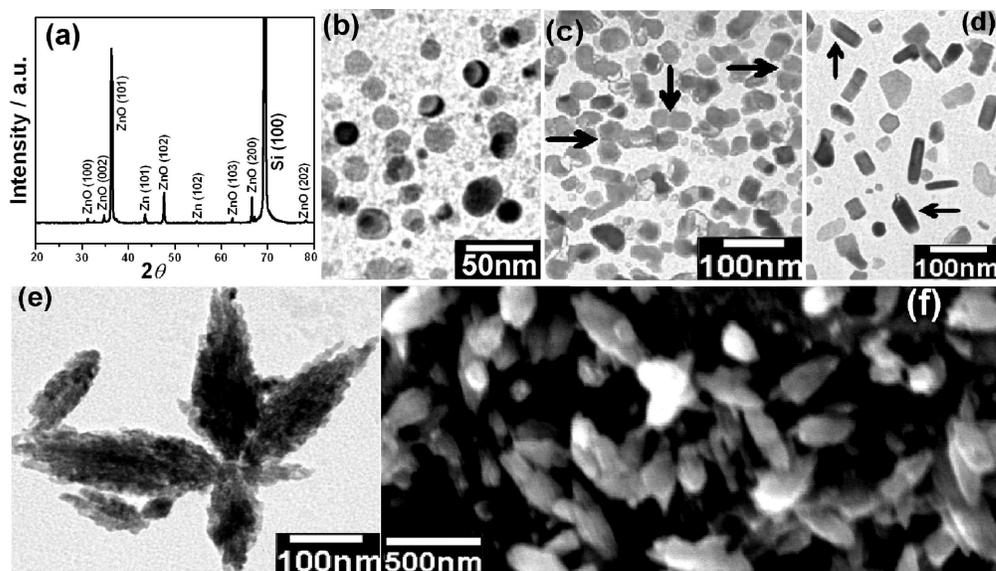

Figure 6.4 (a) Representative XRD pattern for the LP-PLA product (0.01 M SDS, *t* = 2 h). TEM images of the samples for different ablation times (b) 0.5 h, (c) 2 h, (d) 2.5 h, and (e) 5 h. (b) Spherical nanoparticles with a particle size of ~5-25 nm. (c) Adjacent particles that are aligned with one another are highlighted by arrows. (d) Nanorods (highlighted by arrows) which might be formed by NP 1D growth. (e) Well-developed 'leaf-like' structures with rough and dense surfaces. (f) SEM image of ZnO nano-leaf structures prepared by 0.01 M SDS and 5 h ablation times.

For longer ablation times, new 'leaf-like' shapes were observed (width: 230 nm ± 30 nm, length: 770 nm ± 90 nm), as shown in Figure 6.4(e). This image provides evidence of oriented attachment growth, and that the ZnO leaf matrix is composed of many NPs attached side-by-side. A similar phenomenon was also observed by other workers in undoped ZnO NRs, hollow micro-hemispheres [50] and co-doped ZnO nanosheet-based structures [51]. Noticeably, the individual leaf-

like structures within a local region seem to be randomly oriented, while the NPs are aligned preferentially parallel to the *c*-axis along the leaf. Again, it was found that these leaf-like nanostructures are mostly made up of component NPs or NRs, as shown in the SEM image (Figure 6.4(f)).
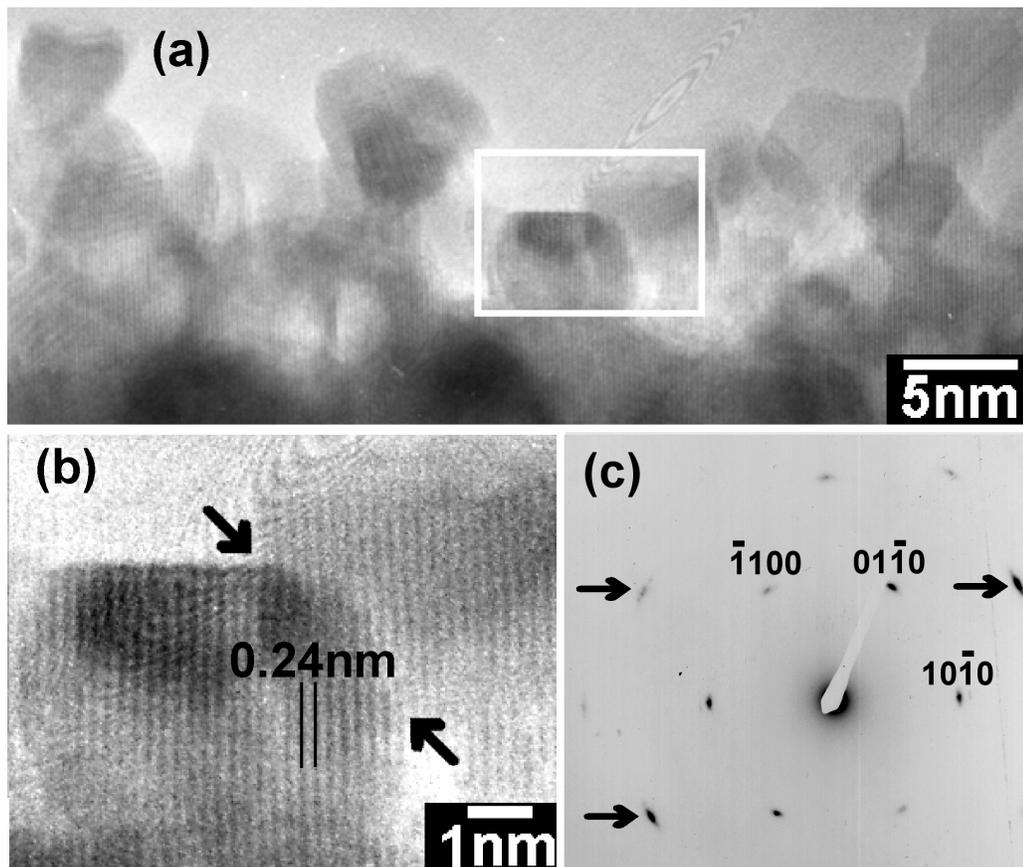

Figure 6.5 (a) HRTEM image of a series of aggregated ZnO NPs. (b) Adjacent particles from the framed area in (a) showing aligned orientations and lattice fringes. The arrows point to the boundaries between the crystallites. (c) SAED pattern taken from the framed area in (a) observed along the [0001] zone-axis, which is consistent with hexagonal symmetry. The arrows point to the curvature of the diffraction spots.

The HRTEM image in Figure 6.5(a) shows that the individual NPs contain very few defects and are primarily faceted with $\{10\bar{1}1\}$ crystal planes (see the enlarged image of the framed area in Figure 6.5(a)), as anticipated from the XRD pattern. The

clear lattice fringes ($d_{10\bar{1}1} = 0.24$ nm) obtained from all crystallites are in good agreement with the values for hexagonal ZnO [48]. The ZnO crystalline NPs that build the leaf-like structures are consistent with an 'oriented attachment' mechanism [52], whereby the adjacent ZnO building units are perfectly aligned with each other in a close orientation relationship, with no mismatch (as shown in Figure 6.5(b), highlighted by arrows between the boundaries. This explains the reason for the slight curvature of the diffraction spots observed in the SAED pattern (Figure 6.5(c), taken from the framed area in (a)).

§ 6.3.2 Controllable growth of ZnO nanostructures

In our experiments, the formation of the distinct leaf-like morphology is very sensitive to the reaction conditions. Concentrations of SDS near the critical micelle concentration (c.m.c. = 0.008 M) and longer ablation times, both favour formation of the leaf-like structures. For lower SDS concentrations (0.001 M) and shorter ablation times (2 h), instead of rod-like particles (as in Figure 6.4(c)), the zinc oxide formed 0D spheres or aligned spheres (Figure 6.6(a-b)). For higher SDS concentrations (0.05 M > c.m.c.) and the same ablation time, the product contained a mixed collection of NPs and NRs (Figure 6.6(c)). Many 0D nanocrystallites have coalesced into straight rod-like structures (shown by the arrows), as further evidence for the proposed growth mechanism. However, on increasing the ablation time to 5 h, the NRs aggregated into leaf-like particles (Figure 6.6(d)). The resulting nanoleaf (width: 200 nm ± 40 nm, length: 500 nm ± 80 nm) are smaller than the ones produced in 0.01 M SDS. This shows that the morphology of the nanostructures is dependant upon the SDS concentration. It is known [53] from studies of $Zn(OH)_2$ NPs that SDS molecules can form a layer directly on a particle surface, which helps to limit the particle size to the nm range. The negatively-charged sulphate groups attach to the positive NP surface, leaving the hydrocarbon tails unbound in the liquid. Close to and above the c.m.c., it becomes energetically favourable for the 'tails' from different NPs to intercalate and form lamella, which effectively 'glue' the NPs together in various packed arrangements. We believe that a similar process is

occurring with our ZnO NPs, leading to self-assembly of the observed nanoleaf structures.
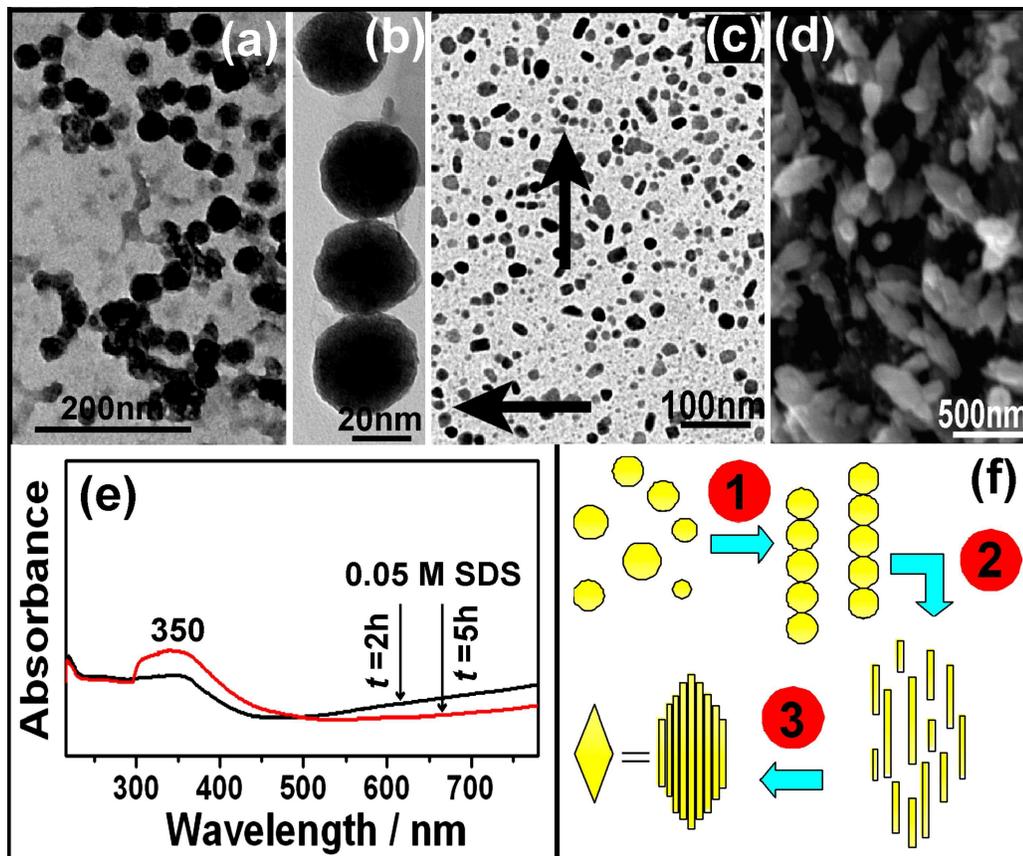

Figure 6.6 (a) and (b) the aligned packing of the NPs (0.001 M SDS, $t = 2$ h). (c) the particles lining up, serving as the starting point for subsequent coalescence into a NR (0.05 M SDS, $t = 2$ h). (d) leaf-like structures (0.05 M SDS, $t = 5$ h). (e) Plot of UV-visible absorbance from the ablation product (0.05 M SDS) for different ablation times, showing a prominent feature at ~350 nm. (f) Proposed model for sequential growth pathway.

Figure 6.6(e) shows the UV-visible optical absorption spectra of the suspensions following different ablation times in 0.05 M SDS. The peak around 350 nm is attributed to the exciton absorption of ZnO [40]. The peak intensity increased with increase of t; however the peak for 2 h has a broad shoulder and is

poorly-defined. Using the value for onset of absorption (where the extrapolation of the steeply-rising part of the absorption spectrum crosses the wavelength axis), the optical (or Tauc) band gap [54] for samples produced after 2 h and 5 h ablation are calculated to be 3.20 and 3.10 eV, respectively. These two values are lower than the value for bulk ZnO (3.37 eV) [49] probably due to quantum confinement effects.

Figure 6.6(f) summarises a suggested mechanism that is consistent with our observations, by which the ZnO particles might self-organize (0D→1D→2D) into the observed complex structures. Such formation behaviors are consistent with previous discussion in Chapter 4.4 about carbon nitride architectures. In general, the high power laser beam causes material to be ejected from the zinc plate predominantly as atomic or ionic species, resulting in the formation of a high temperature, high pressure, and high density (HTHPHD) plasma of evaporated materials. The highly energetic Zn species created within the ablation plume are easily oxidized in such extreme conditions, and then initially condense into small, monodispersed, spherical ZnO NPs. Due to the very short laser pulse length (15 ns) and the fact that the plume is rapidly quenched by the surrounding liquid, the growth times of these nuclei are very short, and so they remain in the nm size range. At a short ablation time, the rate of mesoscale restructuring is relatively low because of insufficient energy input to overcome the restructuring barrier. Thus, the initial products are mainly spherical NPs. However, more complex assembled structures are formed in a longer ablation time (5 h), which has continual energy input to the reaction system and sufficient time for NPs recrystallization. Furthermore, the presence of SDS molecules can form a thin coating around each NP, stabilising them, but also preventing further growth since all the crystal faces will be capped by the surfactant groups. At higher SDS concentrations the tail groups protruding from neighbouring NPs begin to intercalate, thereby minimising the tail-water interactions, and gluing the NPs together. The NPs lying parallel to the *c*-axis are stabilized by SDS to give preferential growth along the [0001] direction. Upon drying of the samples, the strings of NPs coalesce to form the nano-leaf structures. The binding of SDS on the NP surfaces directs their subsequent oriented assembly and growth. This surfactant-mediated restructuring process is consistent with the mechanism proposed by several groups for other materials [55,56]. In general, many surfactants influence

crystal morphology by selective interaction or adsorption on certain faces of the growing crystals, which results in preferential growth along other crystallographic directions. It is still unclear why the NPs form 1D lines rather than random 3D clumps. Further investigations (such as varying the laser fluence, the effect of p*H*, and the conditions for the drying process) are required to elucidate the more detailed aspects of ZnO growth in LP-PLA.

§ 6.3.3 XPS analysis of ZnO nanostructures

X-ray photoelectron spectroscopic studies were carried out in order to examine the surface chemistry of ZnO nanoleaf structures. Figure 6.7(a) and (b) show the typical XPS full spectra of ZnO (a) ablated in 0.001 M SDS for 2 h and (b) an identical sample (a) after annealing for 2 h at 200 C in an oven in air, respectively. The presence of C1*s* peaks appeared at 285 eV for two samples is a consequence of contamination when the samples were exposed to the atmosphere. The O1*s* peak observed at about 530 eV corresponds to O^{2-} for the normal wurtzite structure of ZnO single crystal [57]. There are two peaks at ~1020 and ~1043 eV, which correspond to the binding energies of Zn2$p_{3/2}$ and Zn2$p_{1/2}$, respectively [58]. The binding energies of various core levels match well with the XPS spectrum of bulk ZnO (calibrated by taking the carbon C1*s* peak 284.6 eV as a reference).

Detailed analysis of the ZnO nanostructures were carried out by investigating the Zn-2*p* and O-1*s* core level spectra. As shown in Figure 6.7(c), the intensity of O1*s* increased after annealing for 2 h at 200ºC in air. Oxygen diffuses into the ZnO structure during the annealing and cooling down process in air [59]. At high temperature annealing, large concentration of oxygen vacancies and unsaturated chemical bonds are completely dominated that can combine easily with sufficient Zn atoms to form new ZnO, resulting in the increase of oxygen concentration. The O1*s* signals shown are resolved into two peaks by fitting to Gaussian distributions. The O1 peak, related to O-Zn bonding, is located at 530 eV. The O2 peak, related to OH groups, is located at the higher energy (531.5 eV). The OH group arises from H_2O adsorption and dissociation on the ZnO surface when ZnO nanostructure was annealed at 200ºC.
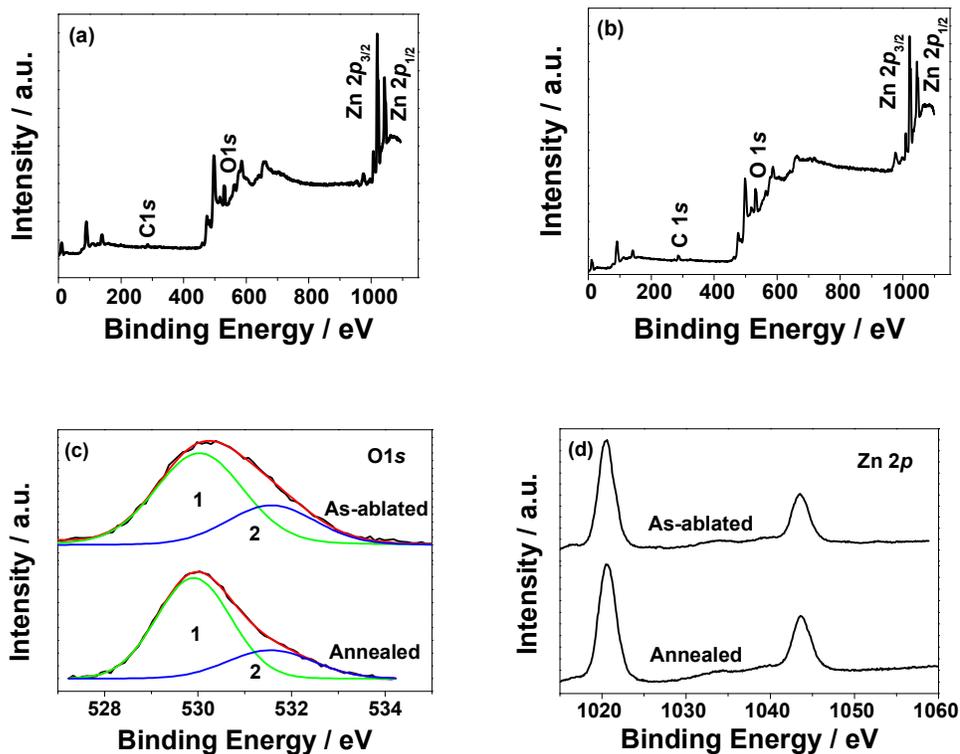
Figure 6.7 XPS survey spectra of ZnO nanostructures (a) sample prepared by 2 h laser ablation with 0.001 M SDS concentrations and (b) sample identical to (a), but after annealling for 2 h at 200 C in an oven in air. (c) Gaussian fitting curves for the O1*s* peaks for the two samples, showing two components (see the discussion in the text). (d) the detailed region scans of Zn 2*p* for two samples.

However, no significant change in either binding energy or shape of the peaks was observed for the Zn-2*p* core level spectra (Figure 6.7 (d)) probably due to the fact that the Zn 2*p* lines are not very sensitive to the chemical environment [60,61].

The atomic concentrations of O and Zn are computed from the measured peak area, together with the following sensitivity factors: O: 0.61; Zn: 4.24. The ratio of O and Zn in the as-ablated ZnO nanophase is 0.64. The ratio of O and Zn in the annealed sample is 0.90, indicating an increase of oxygen atomic concentration. These results are consistent with our observation from the XPS spectra.

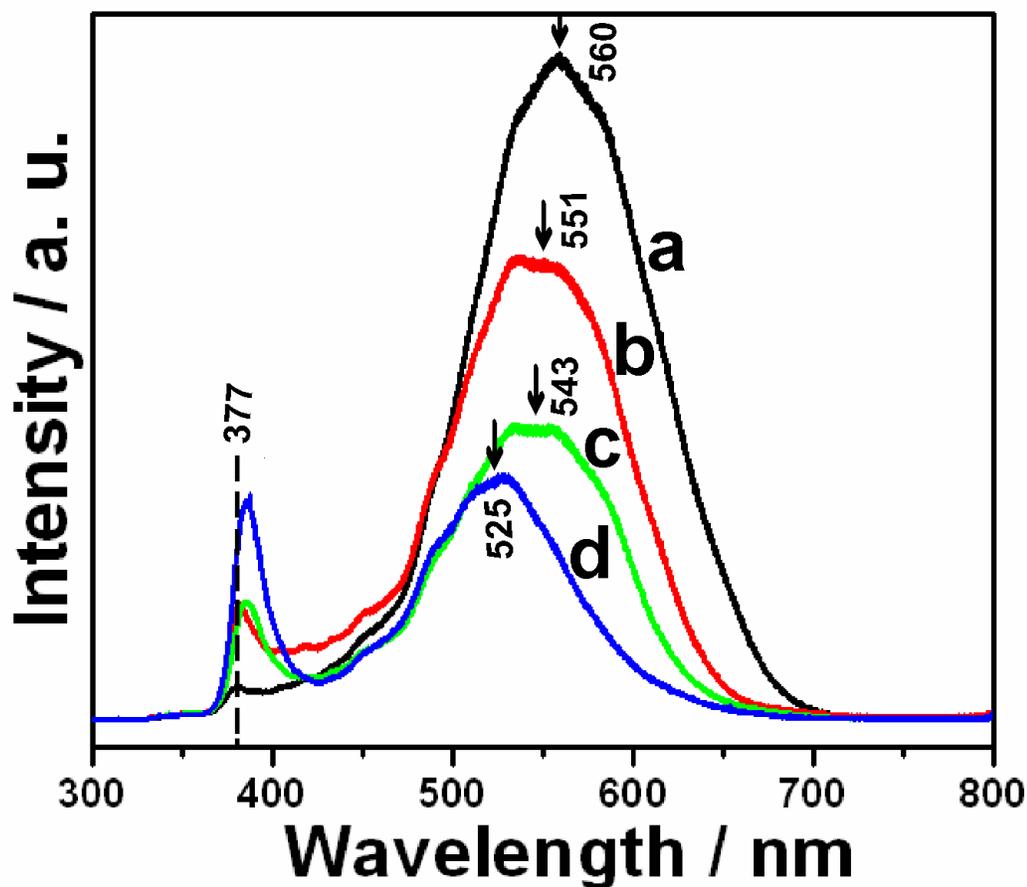### § 6.3.4 Photoluminescence of ZnO nanostructures

Figure 6.8 PL spectra obtained from 325 nm excitation of the sample following 2 h laser ablation with SDS concentrations of: (a) 0.001 M, (b) 0.01 M, and (c) 0.05 M. (d) Sample identical to (a), but after annealling for 2 h at 200ºC in an oven in air.

Figure 6.8 compares room temperature PL spectra from four ZnO samples ablated under different SDS concentrations.   All the spectra show conventional Raman modes similar to those of bulk ZnO and common nanostructured ZnO [62,63]. The ultraviolet (UV) emission is well understood as near-band-edge emission, while the visible emission originates from a variety of deep level defects, *e.g.* vacancies from oxygen and zinc interstitials.   The PL spectrum (Figure 6.8(a)) from the 0.001 M SDS sample shows a small UV emission peak at ~377 nm and a dominant,

broad green/yellow visible emission. The intensity of emission peaks in the blue region increased with increasing SDS concentration, together with a slight red-shift. Conversely, the reduced green emission with the increase of SDS concentration can be attributable to a decrease of oxygen vacancies within the ZnO. This is because SDS molecules can significantly suppress the oxidation rate by forming extremely thin organic layers on the particle surface. The present PL studies indicate that an evolution in ZnO structure (*i.e.* 0D→1D→2D) changed the distribution of UV emission and visible emission intensities. An identical sample (a), after annealing at 200ºC for 2 h showed a large (~6×) increase in the UV emission intensity, and a concomitant quenching of the visible emission. The evident reduction in long wavelength emission intensity from the annealed sample serves to reinforce previous suggestions [64] that oxygen-related defects, such as oxygen interstitials, are responsible for the yellow and red emission.

§ 6.4 Conclusions

Zinc oxide 'nano-leaf' structures have been synthesized at room temperature and pressure using LP-PLA (Nd:YAG 532 nm) of a zinc target in an aqueous solution of sodium dodecyl sulfate (SDS). By controlling the growth kinetics (such as laser irradiance time and the concentration of SDS used for ablation), it is possible to change the growth behaviour of ZnO. The ZnO nanostructures presented in our study include nanoparticles, nanorods, and nanoleaves. It is found that at short ablation times, the initial products are mainly spherical nanoparticles because of insufficient energy input to overcome the restructuring barrier. However, a mixed collection of NPs and NRs or more complex self-assembled nanoleaf structures are formed after a longer ablation time, which has continual energy input to the reaction system and sufficient time for NPs recrystallization. Furthermore, SDS surfactant concentration near the c.m.c. is also favourable in defining the structures observed here. The negative sulphate molecules bond on the surface of the positive NP with the headgroups and the tails formed a layer structure between the particles to reduce the free energy. The pristine particles coated with SDS molecules in close to and

above the c.m.c. condition can effectively glue the NPs together and induce self-assembly nanocrystal in various packed arrangements. The growth mechanism appears to involve an increase of the structural complexity from 0D NPs to 1D NRs, and then broadening of these into 2D 'nano-leaf' structures.

The room temperature photoluminescence spectra from different samples show narrow bandwidth UV emission at ~ 380 nm and strong visible emission, dependent on the conditions. The intensity of emission peaks in the blue region increased with increasing SDS concentration together with a slight red-shift. Conversely, the reduced green emission with the increase of SDS concentration can be attributable to a decrease of oxygen vacancies within the ZnO. PL also confirmed annealling as a good route to improving the intensity of UV emission from the sample, suggesting excellent quality and that these nanocrystals have potential as optoelectronic materials.

The mechanism for production of the zinc oxide nanomaterials involves the following processes: (a) Generation of a high temperature and high-pressure plasma at the solid liquid interface, after interaction between the pulsed laser light and the zinc target. (b) Zinc cluster formation by adiabatic and supersonic expansion leading to cooling of the plasma plume. (c) Interaction of these zinc reactive clusters with species in aqueous solution or oxidation of zinc cluster within the extreme conditions, leading to the formation of ZnO particles.

This work has shown that LP-PLA is an effective method to synthesize a series of ZnO nanomaterials with controlled size and morphology via suitable choice of solid target material and surfactant solution. A thorough understanding of controlled growth (their size, size distribution, shape, crystal structure, and even surface structure) is the key step towards nanosystem applications. With this improved physical and chemical control, solid-solution growth methods should provide versatile and powerful industrial-scale processes for assembling nanomaterials, and may ultimately be moving nanoscience out of the laboratory and into technology.

Bibliography

[1] Keem K, Kim H, Kim G T, Lee J S, Min B, Cho K, Sung M Y, Kim S, *Appl. Phys. Lett.* 2004, **84**, 4376.

[2] Arnold M S, Avouris P, Pan Z W, Wang Z L, *J. Phys. Chem. B*, 2003, **107**, 659.

[3] Wang Z L, *Mater. Today*, 2004, **7**, 26.

[4] Xu W L, Zheng M J, Ding G Q, Shen W Z, *Chem. Phys. Lett.*, 2005, **411**, 37.

[5] Huang M H, Wu Y Y, Feick H, Tran N, Weber E, Yang P D, *Adv. Mater*. 2001, **13**, 113.

[6] Guo L, Ji Y L, Xu H B, Simon P, Wu Z Y, *J. Am. Chem. Soc.*, 2002, **124**, 14864.

[7] Pan Z W, Dai Z R, Wang Z L, *Science*, 2001, **291**, 1947.

[8] Kong X Y, Ding Y, Yang R S, Wang Z L, *Science*, 2004, **303**, 1348.

[9] Zhang J, Sun L D, Liao C S, Yan C H, *Chem. Commun*., 2002, **3**, 262.

[10] Fan H J, Scholz R, Kolb F M, Zacharias M, Gosele U, *Solid State Commun.*, 2004, **130**, 517.

[11] Wen J G, Lao J Y, Wang D Z, Kyaw T M, Foo Y L, Ren Z F, *Chem. Phys. Lett.*, 2003, **372**, 717.

[12] Wang Z L, *J. Phys-Condens. Mat.*, 2004, **16**, R829.

[13] Huang M H, Mao S, Feick H, Yan H Q, Wu Y Y, Kind H, Weber E, Russo R, Yang P D, *Science*, 2001, **292**, 1897.

[14] Zheng M J, Zhang L D, Li G H, Shen W Z, *Chem. Phys. Lett.*, 2002, **363**, 123.

[15] Li Y, Meng G W, Zhang L D, Phillipp F, *Appl. Phys. Lett.*, 2000, **76**, 2011.

[16] Zhang Y, Jia H B, Wang R M, Chen C P, Luo X H, Yu D P, Lee C J, *Appl. Phys. Lett*, 2003, **83**, 4631.

[17] Park W I, Kim D H, Jung S W, Yi G C, *Appl. Phys. Lett.*, 2002, **80**, 4232.

[18] Heo Y W, Norton D P, Tien L C, Kwon Y, Kang B S, Ren F, Pearton S J, LaRoche J R, *Mat. Sci. Eng. R.*, 2004, **47**, 1.

[19] Yi G C, Wang C R, Park W I, *Semicond. Sci. Technol.*, 2005, **20**, S22.

[20] Özgür Ü, Alivov Y I, Liu C, Teke A, Reshchikov M A, Doğan S, Avrutin V, Cho S –J, Morkoç H, *J. Appl. Phys.*, 2005, **98**, 041301.

[21] Zhao M H, Wang Z L, Mao S X, *Nano lett.*, 2004, **4**, 587.

[22] Kulkarni A J, Zhou M, *Appl. Phys. Lett.*, 2006, **88**, 141921.

[23] Volz S G, Chen G, *Appl. Phys. Lett.*, 1999, **75**, 2056.

[24] Sverdrup P G, Ju Y S, Goodson K E, *J. Heat Trans-T Asme*, 2001, **123**, 130.

[25] Li Q H, Wan Q, Liang Y X, Wang T H, *Appl. Phys. Lett.*, 2004, **84**, 4556.

[26] Cao H, Xu J Y, Zhang D Z, Chang S H, Ho S T, Seelig E W, Liu X, Chang R P H, *Phys. Rev. Lett.*, 2000, **84**, 5584.

[27] Özgür Ü, Teke A, Liu C, Cho S J, Morkoç H, Everitt H O, *Appl. Phys. Lett.*, 2004, **84**, 3223.

[28] Bagnall D M, Chen Y F, Zhu Z, Yao T, Shen M Y, Goto T, *Appl. Phys. Lett.*, 1998, **73**, 1038.

[29] Kind H, Yan H Q, Messer B, Law M, Yang P D, *Adv. Mater.*, 2002, **14**, 158.

[30] Johnson J C, Knutsen K P, Yan H Q, Law M, Zhang Y F, Yang P D, Saykally R J, *Nano lett.*, 2004, **4**, 197.

[31] Fan Z Y, Chang P C, Lu J G, Walter E C, Penner R M, Lin C H, Lee H P, *Appl. Phys. Lett.*, 2004, **85**, 6128.

[32] Wan G, Li Q H, Chen Y J, Wang T H, He X L, Li J P, Lin C L, *Appl. Phys. Lett.*, 2004, **84**, 3654.

[33] Kang B S, Heo Y W, Tien L C, Norton D P, Ren F, Gila B P, Pearton S J, *Appl. Phys. A*, 2005, **80**, 1029.

[34] Rout C S, Krishna S H, Vivekchand S R C, Govindaraj A, Rao C N R, *Chem. Phys. Lett.*, 2006, **418**, 586.

[35] Baratto C, Sberveglieri G, Onischuk A, Caruso B, di Stasio S, *Sensor. Actuat. B*, 2004, **100**, 261.

[36] Kim J S, Park W I, Lee C H, Yi G C, *J. Korean Phys. Soc.*, 2006, **49**, 1635.

[37] Sarvari M H, Sharghi H, *Tetrahedron*, 2005, **61**, 10903.

[38] Daneshvar N, Salari D, Khataee A R, *J Photoch. Photobio. A*, 2004, **162**, 317.

[39] Usui H, Shimizu Y, Sasaki T, Koshizaki N, *J. Phys. Chem. B*, 2005, **109**, 120.

[40] Zeng H B, Cai W P, Cao B Q, Hu J L, Li Y, Liu P S, *Appl. Phys. Lett.*, 2006, **88**, 181905.

[41] Liu J P, Huang X T, Li Y Y, Sulieman K M, Sun F L, He X, *Scripta Mater.*, 2006, **55**, 795.

[42] Liu B, Zeng H C, *J. Am. Chem. Soc.*, 2004, **126**, 16744.

[43] Yang L, May P W, Yin L, Brown R, Scott T B, *Chem. Mater.*, 2006, **18**, 5058.

[44] Yang L, May P W, Yin L, Scott T B, Smith J A, Rosser K N, *Nanotechnology*, 2006, **17**, 5798.

[45] Yang L, May P W, Yin L, Smith J A, Rosser K N, *J. Nanopart. Res.,* 2007, 9, 1181.

[46] Yang L, May P W, Huang Y Z, Yin L, *J. Mater. Chem.*, 2007, **17**, 1255.

[47] Burke S E, Eisenberg A, *Langmuir*, 2001, **17**, 8341.

[48] Liu B, Zeng H C, *J. Am. Chem. Soc.*, 2003, **125**, 4430.

[49] Zeng H B, Cai W P, Li Y, Hu J L, Liu P S, *J. Phys. Chem. B*, 2005, **109**, 18260.

[50] Mo M, Yu J C, Zhang L Z, Li S K A, *Adv. Mater.*, 2005, **17**, 756.

[51] Wang X F, Xu J B, Ke N, Yu J G, Wang J, Li Q, Ong H C, Zhang R, *Appl. Phys. Lett.*, 2006, **88**, 223108.

[52] Penn R L, Banfield J F, *Science*, 1998, **281**, 969.

[53] Sasaki T, Shimizu Y, Koshizaki N, *J Photoch. Photobio. A*, 2006, **182**, 335.

[54] Tauc J, *Amorphous and liquid semiconductors* (London and New York: Plenum), 1974, p.171.

[55] Yu J G, Zhao X F, Liu S W, Li M, Mann S, Ng D H L, *Appl. Phys. A*, 2007, **87**, 113.

[56] Chen D, Shen G Z, Tang K B, Liang Z H, Zheng H G, *J. Phys. Chem. B*, 2004, **108**, 11280.

[57] Coppa B J, Davis R F, Nemanich R J, *Appl. Phys Lett.*, 2003, **82**, 400.

[58] Wei X Q, Man B Y, Liu M, Xue C S, Zhuang H Z, Yang C, *Physica B*, 2007, **388**, 145.

[59] Mar L G, Timbrell P Y, Lamb R N, *Thin Solid Film*, 1993, **223**, 341.

[60] Lindsay R, Thornton G, *Top. Catal.*, 2002, **18**, 15.

[61] Rössler N, Kotsis K, Staemmler V, *Phys. Chem. Chem. Phys.*, 2006, **8**, 697.

[62] Sun Y, Fuge G M, Fox N A, Riley D J, Ashfold M N R, *Adv. Mater.*, 2005, **17**, 2477.

[63] Zhang Y, Jia H B, Wang R M, Chen C P, Luo X H, Yu D P, Lee C J, *Appl. Phys. Lett.*, 2003, **83**, 4631.

[64] Cross R B M, De Souza M M, Narayanan E M S, *Nanotechnology*, 2005, **16**, 2188.